Spin-Coating-Free Deposition of ZnO and RGO@ZnO Nanolayers for Efficient, Economical Perovskite Solar Cells

Ayça Tanrıverdi[1,2]†

[1]*Vocational School of Health Services, Dept. of Opticianry, Kahramanmaras Sutcu Imam University, Kahramanmaras, Turkey*

[2]*Department of Material Science and Engineering, Graduate School of Natural and Applied Sciences, Kahramanmaras Sutcu Imam University, Kahramanmaras, Turkey*

† Corresponding Author Name-Surname: Ayça Tanrıverdi (https://orcid.org/0000-0002-0658-8576) **aycatanriverdi@ksu.edu.tr**

Abstract

In this study, ZnO nanoparticles (NPs) and RGO@ZnO nanocomposites (NCs) were integrated as electron transport layers (ETLs) using spin-coating-free deposition methods and cost-effective and scalable fabrication of planar perovskite solar cells was achieved. ZnO NPs and RGO@ZnO NCs were synthesized via a rapid hydrothermal process and characterized using XRD, SEM, UV-Vis, and FTIR techniques. Structural and optical analyses confirmed the formation of highly crystalline and uniform nanostructures, with RGO integration enhancing light absorption and narrowing the band gap. The films were deposited using the doctor blade technique, and the $MAPbI_3$ perovskite layer was formed by a simple drop-casting method. PCBM was used as the hole transport layer, and a silver (Ag) paste was applied as the top electrode. Photovoltaic performances of two device structures, ITO/ZnO/$MAPbI_3$/PCBM/Ag and ITO/RGO@ZnO/$MAPbI_3$/PCBM/Ag, were compared. Devices incorporating RGO@ZnO exhibited significantly improved efficiency up to threefold under standard solar illumination due to reduced charge recombination, improved energy level alignment, and enhanced carrier mobility. Moreover, these devices maintained high performance under indoor LED lighting, demonstrating superior low-light adaptability.

Keywords: Perovskite solar cell; Hydrothermal method; RGO@ZnO Nanocomposites; Electron transport layer; Spin-coating-free deposition.

1. Introduction

Most of the energy used today is generated using fossil fuels, such as oil, gas and coal, which become increasingly scarce. But fossil fuel reserves are dwindling every day. Inevitably, however, energy consumption increases in line with population growth, urbanisation, industrialisation, the spread of technology and rising prosperity. Interest in renewable energy sources is on the rise as the demand for energy continues to grow. Solar energy, a limitless

source of energy, is easily converted into electricity using photovoltaic solar panels. Due to their remarkable features such as high efficiency and low cost, perovskite solar cells (PSCs) are attracting a lot of attention among photovoltaic solar cells. Perovskite solar cells are a new technology to collect and convert solar energy [1,2]. Synthetically produced and used in solar cells, perovskite is a natural mineral structure [3,4]. Perovskite materials are more economical to manufacture and use than conventional solar cells [5]. The crystal structure of perovskite materials is ABX_3. Position A contains an organic cation, B is metal cation and X is halide anion [6–8]. Typically located between the electron transport layer (ETL) and the hole transport layer (HTL), this perovskite layer is responsible for light harvesting [9]. Although this structure was discovered in the 19th century, it has only recently been successfully used in photovoltaics [10].

Graphene, a widely studied carbon allotrope, has garnered significant attention in both scientific research and industry due to its exceptional physical and chemical properties [11]. As one of the rare two-dimensional planar nanomaterials, graphene exhibits a remarkably high theoretical specific surface area (2630 $m^2\ g^{-1}$), outstanding intrinsic carrier mobility (200,000 $cm^2\ V^{-1}\ s^{-1}$), excellent optical transmittance (~97.7%), and superior electrical and thermal conductivity, making it a versatile material for various advanced applications [12]. Moreover, it can be synthesized through cost-effective chemical methods and possesses abundant surface functional groups, further enhancing its processability and integration into composite systems [13].

In recent years, reduced graphene oxide (RGO)/metal oxide composites have emerged as multifunctional materials used across a broad spectrum of scientific disciplines. Among metal oxides, zinc oxide (ZnO) stands out as a particularly promising semiconductor, owing to its Wurtzite crystal structure, wide bandgap (~3.37 eV), and favorable light absorption characteristics [14]. ZnO is especially attractive for use in electron transport layers (ETLs) of perovskite solar cells (PSCs) due to its low toxicity, affordability, and excellent optoelectronic properties [15].

In recent years, several studies have demonstrated significant advancements in the use of graphene and ZnO-based materials as ETLs in PSCs. Khan and Han (2022) reported that incorporating reduced graphene oxide (rGO) into ZnO ETLs improved charge transfer at the perovskite/ETL interface, suppressing recombination and enhancing the power conversion efficiency (PCE) from 15.93% to 17.08% [16]. Eswaramoorthy and Rajaram (2023) introduced 1D g-C_3N_4 additives blended with ZnO ETLs, which reduced surface defects, improved electron extraction, and achieved a maximum PCE of 12.22% under ambient conditions [17]. Chaudhary and et al. (2024) demonstrated that combining a graphene oxide (GO) hole transport layer with

ZnO-based ETLs in Sn-based PSCs yielded a simulated PCE of 22.24% while maintaining high temperature stability and low environmental impact [18]. More recently, Chauhan and et al. (2025) incorporated graphene quantum dots (GQDs) into ZnO ETLs, resulting in enhanced interfacial charge transfer, improved perovskite crystallinity, and a record PCE of 20.23% with superior stability compared to pristine ZnO-based PSCs [19]. These recent advancements highlight the critical role of metal oxide-based ETLs in enhancing PSC performance, motivating further exploration of synthesis techniques and device architectures. Consequently, metal oxide-based materials have attracted significant attention in perovskite solar cell research, owing to their efficient charge transport, structural stability, and suitability for low-temperature, solution-based fabrication methods. A variety of synthesis techniques such as microwave-assisted methods [20], microemulsion [21], electrodeposition [22], sol-gel [23], green synthesis [24], and hydrothermal/solvothermal routes [25] have been developed to prepare metal oxide nanomaterials. Among these, hydrothermal synthesis is particularly notable for its simplicity, cost-effectiveness, and ability to produce homogeneous, high-purity materials in an environmentally friendly manner.

This study investigates the photovoltaic performance of planar perovskite solar cells using ZnO and RGO@ZnO nanocomposites as electron transport layers (ETLs). Both materials were synthesized via a simple and economical hydrothermal method and characterized by XRD, SEM, UV-Vis, and FTIR analyses. Methylammonium lead iodide ($MAPbI_3$) served as the light-absorbing perovskite layer, with its precursor MAI synthesized in the laboratory. Device structures of ITO/ZnO/$MAPbI_3$/PCBM/Ag and ITO/RGO@ZnO/$MAPbI_3$/PCBM/Ag were fabricated using spin-coating-free techniques such as doctor blade and drop casting. Silver paste was applied as the top contact. Photovoltaic parameters including *Voc, Jsc, FF,* and PCE were evaluated, showing enhanced efficiency in devices using RGO@ZnO ETLs.

2. Experimental

2.1. Synthesis of ZnO NPs

0.1 M zinc nitrate hexahydrate ($Zn(NO_3)_2$-$6H_2O$) was dissolved separately in 50 ml DI water and 0.1 M hexamethylenetetramine (HMT, $C_6H_{12}N_4$) in 50 ml DI water. Both solutions were combined and stirred on a magnetic stirrer for 10 minutes. The solution was then placed in a teflon-lined autoclave and kept in a muffle furnace at 160°C for 3 h for the synthesis of $Zn(OH)_2$ particles. $Zn(OH)_2$ particles were filtered from the solution that had cooled at room temperature. In order to remove organic components, the $Zn(OH)_2$ particles were washed 3 times with deionised water. The synthesised $Zn(OH)_2$ particles were annealed in a muffle furnace at 450

°C for 1 h to eliminate the hydroxide phase in the structure. Figure 1 shows a schematic of the production processes and experimental mechanisms of ZnO particles.

2.2. Synthesis of RGO@ZnO NPs

The hydrothermal method was used to prepare RGO@ZnO composites. GO was synthesised from natural graphite powders by a modified Hummers method as described previously [26]. Graphene oxide (GO) used in this study was synthesized in a study conducted by us before, and its structural and morphological properties were examined in detail in that study [27]. Therefore, synthesis and characterization information regarding GO is not included again in this study. 0.1g GO prepared according to Hummers' method was mixed with 20 ml DI water and 10 ml ethanol (C_2H_5OH). To dissolve the GO, it was placed in an ultrasonic bath for 1 hour. Subsequently, 0.1 g of ZnO powder was added to this solution and kept in an ultrasonic bath for 2 hours. The solution was placed in a Teflon autoclave and kept in a muffle furnace for 3 hours at 160ºC. The RGO@ZnO nanocomposite was synthesized to contain 20 wt% reduced graphene oxide [27,28]. So, both reduced GO and chemically bound RGO@ZnO composites were obtained [29]. For the synthesis of RGO@ZnO nanocomposites, the obtained composite material was filtered, washed with deionised water and dried at room temperature.

2.3. Synthesis of MAI

24 ml of methylamine (CH_3NH_2) was stirred in an icebath. 12 ml hydriodic acid (HI) was added drop by drop. The mixture was stirred for 2 hours in an ice bath (0ºC). It was observed that the colour of the solution was homogeneous and light yellow. Solution removed from ice bath and kept at room temperature [30]. Then, by lowering the boiling point (vapour pressure) of the solutions, a rotary evaporator was used to evaporate the solution at lower temperatures than required. The MAI salt obtained was washed three times with ether and ethanol.

2.3. Fabrication of PSC

In this study, monolayer planar perovskite solar cells have been fabricated using ITO/ZnO/$MAPbI_3$/PCBM/Ag and ITO/RGO@ZnO/$MAPbI_3$/PCBM/Ag device structures. The PSC was fabricated using a 10 Ω/sq indium-doped tinoxide (ITO) glass substrate. ITO glass substrates have been cleaned with detergent, ethanol and ultrapure water and oven dried for 10 minutes. 0.25 M ZnO nanoparticles, prepared by the hydrothermal method, were mixed in ethanol to form a homogeneous paste. The electron transport layer was created by depositing a thin layer of paste on the ITO substrate. This was done using the doctor blade method. It was prepared by separately mixing 20 mg commercial lead iodide (PbI_2) in 1 mL dimethylformamide (DMF) and 40 mg MAI in 1 mL isopropanal. A perovskite solution was formed by mixing of PbI_2 and MAI solutions in a ratio of 1:2. Then, by the dropping method,

150 µl of $MAPbI_3$ solution and 50 µl of anhydrous chlorobenzene solvent were dropped onto the central surface of the ZnO layer. The $MAPbI_3$ layer was then annealed at 100 °C for 10 min. The light absorbing perovskite layer was formed. The HTL solution was prepared by dissolving 25 mg of PCBM (butyric methyl ester) organic salt in 1 mL of chlorobenzene. The prepared HTL solution was deposited on the ITO / ZnO / $MAPbI_3$ coated film by a simple drop technique. Following film deposition, formal thickness measurements were not conducted; however, film uniformity was evaluated visually, and only samples exhibiting apparent homogeneity were selected for device fabrication and testing. Finally, the perovskite solar cell fabrication was completed by making silver (Ag) contacts. In this way, a perovskite solar cell with an ITO/ZnO/$MAPbI_3$/PCBM/Ag device structure was obtained, while perovskite solar cells with an ITO/RGO@ZnO/$MAPbI_3$/PCBM/Ag configuration were fabricated using the same processing steps (Figure 2).

3. Characterization

The structural and optical characterizations of the synthesized materials were carried out using various analytical techniques. X-ray diffraction (XRD) patterns were recorded with a Philips X'Pert Pro diffractometer employing Cu-Kα radiation (λ = 0.154 nm). Fourier-transform infrared (FT-IR) spectra were obtained using a Perkin Elmer 400 FT-IR spectrometer, while UV–Vis absorption spectra were recorded with a Shimadzu UV-1800 spectrophotometer. Surface morphology was examined using a Zeiss EVO 10LS scanning electron microscope (SEM). All characterizations were conducted at the University–Industry–State Cooperation Centre (USKIM) of Kahramanmaras Sutcu Imam University.

3.1. Characterization of ZnO NPs and RGO@ZnO NCs

The characterization of ZnO and RGO@ZnO nanoparticles was performed using XRD, SEM, and UV-Vis spectroscopy. The diffraction patterns of ZnO NP and RGO@ZnO NC are compared in the XRD pattern given in Figure 3. The diffraction pattern of ZnO NPs includes the characteristic diffraction peaks of ZnO, which has a hexagonal wurtzite structure. The diffraction pattern peaks of ZnO NPs were found as 2θ=31.71º, 34.35º, 36.17º, 47.45º, 56.51º, 62.75º, 66.27º, 67.85º, and 69.03º. The planes corresponding to these angular values are (100), (002), (101), (102), (110), (103), (200), (112), and (201), respectively. These peaks are consistent with JCPDS card no 01-079-2205 [31], indicating that ZnO is well crystallized. The observation of the characteristic peaks belonging to ZnO in the RGO@ZnO sample also demonstrates that the crystal structure of ZnO is preserved in the composite structure and no phase transformation occurs [32]. However, it has been observed that all peak intensities decrease in RGO@ZnO NCs compared to ZnO. This decline may be attributable to the fact that

the composite with RGO impedes the crystal growth of ZnO to a certain extent, or that the RGO layers partially envelop the ZnO crystals, thereby attenuating the X-ray signals. Additionally, given the amorphous nature of RGO, it exhibits no discernible XRD peaks. This observation lends further support to the hypothesis that no crystal structure is formed in graphene and that it becomes a composite with the ZnO matrix in a homogeneous distribution. While the presence of RGO does not induce a substantial change in the orientation of the ZnO crystals, it does result in a decrease in the crystallinity degree of ZnO [33]. This phenomenon became particularly evident in the high-density ZnO peaks, such as the (101) plane. This outcome indicates the successful loading of ZnO particles onto the RGO surface, thereby synthesizing the composite structure.

SEM images of the prepared ZnO NPs and RGO@ZnO NCs are shown in Figure 4(a-b). SEM analyses revealed that the synthesized ZnO nanostructures were predominantly formed as hexagonal rods, but exhibited a distinct morphological diversity. Within the ZnO structures, nanorods (NR) and hollow nanotubes (NT) with lengths of about 500 nm-1 µm and diameters of 50-100 nm coexist. These structures exhibited a high level of structural organization, forming flower-like clusters 3-5 µm in diameter (Figure 4a). This dual morphology indicates that the synthesis conditions play a decisive role in the shape and growth direction of ZnO crystals. This morphological diversity was found to provide significant advantages in applications requiring high surface interactions such as electronics by increasing the surface area.

The SEM image presented in Figure 4b confirmed the successful synthesis of the RGO@ZnO nanocomposite. In the magnified area, ZnO nanostructures were observed to be homogeneously dispersed on the RGO layers, which had a thickness of several nm. The ZnO particles were found to vary in size from approximately 30 to 80 nm and were found to interact with the RGO surface. It was also observed that these particles have a propensity to self-assemble into NRs or NTs. This hybrid structure combines the high conductivity and surface area of RGO with the functional properties of ZnO.

Figure 5 presents comparative UV-Vis absorbance spectra of pure (a) ZnO NPs and (b) RGO@ZnO NCs. Both materials exhibit absorbance in the 300–700 nm range. However, the spectra's distinctive features clearly reflect the materials' structural differences and the impact of RGO on their optoelectronic properties. ZnO NPs exhibit a distinctive absorbance edge at approximately 370 nm, representing the band gap transition of ZnO. The RGO@ZnO nanocomposite exhibits higher overall absorbance and a more pronounced increase in absorbance compared to ZnO, especially at short wavelengths (~300–400 nm) [34]. This can be attributed to graphene-derived RGO's light absorption enhancement effect due to its large

surface area, high carrier mobility, and π–π* transitions. The increased absorbance in the RGO@ZnO spectrum indicates an increased light-collecting ability of the composite material in the UV and visible regions. This increase is particularly advantageous for optoelectronic applications. Additionally, the literature frequently reports that the recombination of electron-hole pairs decreases as a result of integrating RGO onto the ZnO surface, thus improving optical performance.

Figure 6 shows the band gap values of ZnO NPs and RGO@ZnO NCs, which were determined using the Tauc method and presented comparatively. This graph plots the relationship between $(\alpha h\nu)^2$ and photon energy $h\nu$ based on the Tauc equation, which is valid for direct band transition semiconductors (Eq. 1) [35].

$$(\alpha h\nu)^2 = A(h\nu - Eg) \quad (1)$$

The graph illustrates the relationship between $(\alpha h\nu)^2$ and photon energy $h\nu$, as predicted by the Tauc equation. This equation is applicable to direct band transition semiconductors. The band gap (Eg) value of ZnO was found to be 2.82 eV, reflecting its characteristic direct band gap. Conversely, the band gap value of RGO@ZnO NCs was found to be 2.68 eV [36]. This visible band narrowing is the result of ZnO modification with RGO, indicating changes in the NCs electronic structure. Integrating RGO into the ZnO structure increases the carrier density and forms localized intermediate energy levels, thus narrowing the band gap. The conductive π-conjugated structure of RGO, in particular, allows for the formation of new energy levels between ZnO valence and conduction bands. This increases the materials light absorption capacity in the visible region by shifting photon absorption to lower-energy photons. This feature makes RGO@ZnO NCs advantageous for light-sensitive technologies, such as photovoltaic applications.

3.2. Methylammonium Iodide (MAI) Characterization

MAI particles were characterized using XRD, SEM, and UV-Vis spectroscopy (Figure 7 a-d) . Figure 7(a) shows the X-ray diffraction (XRD) pattern of the Methylammonium Iodide (MAI) compound. The graph includes diffraction data obtained in the 2θ range of 10°–70°. As can be seen, the MAI compound exhibits distinct, sharp diffraction peaks, which indicates a high degree of crystallinity and a regular atomic arrangement. The high-intensity peaks at 2θ ≈ 14.2°, 28.4°, and 31.8°, corresponding to the (002), (003), and (112) planes, respectively, are especially notable in the XRD pattern. These peaks are characteristic of the tetragonal crystal system of MAI and align with standard diffractograms reported in the literature. Additionally, although they are less intense, diffraction signals belonging to the (110), (102), (200), (113), (211), (104), (203), (005), (222), and (115) planes are also present in the spectrum. These

signals reflect the contribution of different crystal orientations of the sample and indicate the presence of a polycrystalline structure. XRD analysis shows that the MAI compound has high crystallinity and well-defined phase purity [37]. These crystal structures are important because they provide the desired electron and hole transport properties in perovskite-based photovoltaic devices. Therefore, the results confirm that MAI is a high-quality precursor for synthesizing perovskite structures. Figure 7b shows an SEM image of the MAI synthesized under laboratory conditions. The image reveals that the MAI particles are homogeneously distributed on the surface and have irregular morphologies. The particles tend to agglomerate due to the hygroscopic nature and crystallization conditions of MAI [38]. In the magnified region, the crystal structure formed on the surface is clearly visible, exhibiting various sizes and a protruding morphology. These irregular structures indicate the low degree of crystallinity characteristic of MAI synthesized by the precipitation method. The morphological properties of MAI can directly affect the homogeneity of the film and the quality of the final perovskite crystal. Effect of CH_3NH_3I vapour evaporation temperature on the quality of the lead-free bismuth based perovskites thin-films. Figure 7c shows the UV-visible (UV-Vis) absorbance spectrum of the synthesized MAI solution. The spectrum, which was measured within the wavelength range of 300–700 nm, shows a high absorbance value around 300 nm. This indicates the strong UV absorption feature of MAI. There is a rapid decrease in absorbance between 320 and 400 nm. Beyond 400 nm, the spectrum remains relatively flat and approaches minimum absorbance. This trend indicates that MAI is a wide-bandgap material with very low light absorption in the visible region. The optical bandgap of MAI was determined using the Tauc graph in Figure 7d. The band gap value was found to be approximately 2.94 eV (Eq 1). It is important to clarify that this measurement pertains to the MAI precursor material alone and does not represent the bandgap of the final $MAPbI_3$ perovskite absorber. This distinction emphasizes that MAI serves as a precursor rather than the light-absorbing layer in the device. The high bandgap indicates that MAI plays an important role as a perovskite precursor rather than a light-absorbing layer and provides advantages in terms of light transmittance in optoelectronic applications. MAI's structural and optical properties confirm its suitability for targeted photovoltaic applications and support its use as a basic building block in producing perovskite layers in the next stage.

3.3. Photovoltaic performance

Device testing was conducted under well-defined illumination conditions to ensure accurate performance evaluation. A Luzchem Xenon Photoreactor equipped with a 300 W xenon arc

lamp was employed as a broad-spectrum solar simulator. For indoor measurements, a commercially available 100 W white LED light source (approx. 33 W/m², 10,000 lumens) was used. All experiments were conducted using the same active area. The efficiency of a solar cell can also be evaluated by the fill factor (*FF*) and power conversion efficiency (PCE, η%). The calculation of *FF* involves the division of the maximum possible power output of a cell by the product of open circuit voltage and short circuit current [39]. The performance of a solar cell in converting solar energy into electrical energy is measured by its PCE. PCE of a photovoltaic cell can be calculated by dividing its maximum possible power output by the incident power intensity from the light source [39].

$$FF = \frac{J_m \times V_m}{J_{sc} \times V_{oc}} \tag{2}$$

$$(\eta\ \%) = \frac{J_{sc} \times V_{oc} \times FF}{P_{in}} \times 100 \tag{3}$$

Figure 8(a-b) shows the current-voltage (J–V) and power-voltage (P–V) characteristics of perovskite solar cell fabricated using an ITO/ZnO/$MAPbI_3$/PCBM/Ag device architecture. The ZnO NPs are used as the electron transport layer (ETL) in the device. The measurements were carried out under two different illumination conditions: Solar simulator [40] and LED light source [41]. The J–V curve (Figure 8a) showed an energy conversion efficiency of 6.45%, with a short-circuit current (*Jsc*) of 17.33 mA/cm² and a voltage (*Voc*) of 1 V under solar simulation. Performance under LED illumination was lower, with a *Jsc* of 14.63 mA/cm² and a *Voc* of 0.98 V (4.88%). This may be due to the LED's spectral distribution being less effective in absorbing the perovskite material. Similarly, the P-V characteristics (Figure 8b) show that the device achieves its maximum power output under the solar simulator. The maximum power point (MPP) occurs around 0.7 V. The peak power density obtained under solar simulation is significantly higher than that obtained under LED illumination. While the device operating under LED illumination exhibits significant power generation, this value is lower than that of solar simulation. The data in the graphs shows that the ZnO NP structure of the device acts as an effective electron transport layer (ETL) and forms a successful heterojunction with the perovskite layer.

The photovoltaic performance of the perovskite solar cell with an ITO/RGO@ZnO/$MAPbI_3$/PCBM/Ag configuration was evaluated using solar simulator and LED illumination. The current-voltage (*J-V*) (Figure 9a) and power-voltage (*P-V*) curves (Figure 9b) comparatively reveal the efficiency obtained from both light sources. Measurements

made under the solar simulator show that the perovskite solar cell exhibits high performance. The device provided an energy conversion efficiency of 17.93%, with *Jsc* of 22.24 mA/cm² and *Voc* of 1 V. These values show that the RGO-doped ZnO layer significantly increases carrier transport and collection capacity, as well as reducing recombination losses by improving energy matching at the interfaces. Measurements under the LED light source show that the device has a performance of 20.86 mA/cm² *Jsc* and 0.99 V *Voc*. Despite the lower intensity of the LED light compared to the solar simulator, the device has proven capable of performing effective energy conversion under indoor lighting, achieving an efficiency of 6.50%. These results demonstrate that the device can be used in both outdoor and indoor conditions. The photovoltaic parameters of the perovskite solar cells with ZnO and RGO@ZnO ETLs are presented in Table 1. The photovoltaic performance of devices incorporating ZnO NPs and RGO@ZnO NCs was systematically evaluated under both solar simulator and LED illumination (Table 1). Under solar simulator illumination, the RGO@ZnO-based device exhibited a significantly higher PCE (17.93%) and *FF* (0.80) compared to the ZnO NP-based device (PCE = 6.45%, *FF* = 0.37), indicating enhanced charge transport and reduced recombination resulting from the incorporation of RGO. In contrast, under LED illumination, the same RGO@ZnO device showed a lower *FF* (0.31) and PCE (6.50%), which can be attributed to differences in light intensity and spectral distribution that affect carrier extraction. These results demonstrate that RGO modification effectively improves electron transport efficiency and mitigates recombination, consistent with the observed enhancement in device performance under standard illumination conditions. The pronounced decrease in the *FF* of the RGO@ZnO-based device under LED illumination (0.80 → 0.31) can be primarily attributed to the strong influence of parasitic resistive losses at low light intensities. Under reduced photocurrent generation, even minor leakage pathways (low shunt resistance) or interfacial defects become dominant, leading to a flattening of the J–V curve and, consequently, a significant reduction in *FF*. In addition, spectral differences between the LED source and the solar simulator may shift the carrier generation profile within the perovskite absorber, thereby enhancing interfacial [42]. In addition, the higher efficiency and *FF* observed under the solar simulator compared to the LED source can be mainly explained by differences in illumination intensity and spectral distribution. The solar simulator provides an irradiance close to the standard AM 1.5G spectrum (≈100 mW/cm²) with good uniformity, which enables higher photocurrent generation and efficient carrier extraction. In contrast, the LED source delivers lower irradiance and a narrower spectral output.

Under reduced illumination intensity, parasitic resistive losses become more pronounced [43]. Shunt pathways and interfacial defects that are negligible under strong illumination can dominate the device response at lower current densities, leading to a flattening of the J–V curve and a pronounced decrease in *FF*. Similarly, series resistance and contact-related barriers exert a stronger relative influence at low light levels, further lowering the *FF*.

In support of the observed *FF* in our RGO@ZnO-based device, similar trends have been reported in the literature for ZnO/graphene composites used as electron transport layers. For instance, Nghia et al. synthesized ZnO/rGO composites for dye-sensitized solar cells and reported an *FF* of 0.70, highlighting the beneficial role of reduced graphene oxide in improving charge transport and interfacial properties [44]. Likewise, Tavakoli et al. demonstrated that incorporating monolayer graphene (MLG) at the ZnO/perovskite interface, together with perovskite passivation, significantly enhanced both the efficiency and stability of perovskite solar cells. Their devices achieved a maximum *FF* of 78.1% along with a PCE exceeding 21%, while also maintaining more than 90% of the initial efficiency after 300 h of continuous illumination [45].

Conclusion

In this study, comparative research was conducted on two perovskite solar cell configurations, ITO/ZnO/$MAPbI_3$/PCBM/Ag and ITO/RGO@ZnO/$MAPbI_3$/PCBM/Ag, to evaluate the effect of RGO integration on device performance. Structural and optical characterizations of ZnO and RGO@ZnO layers confirmed the successful formation of highly crystalline nanostructures with enhanced light absorption and narrowed band gaps, especially in RGO-integrated NPs. RGO integration significantly improved the optoelectronic properties by reducing defect densities, increasing electron mobility, and facilitating more efficient charge extraction at the ETL/perovskite interface. Photovoltaic measurements under both solar simulator and LED illumination revealed a significant increase in power conversion efficiency in RGO@ZnO-based devices compared to their conventional ZnO counterparts. The device using RGO@ZnO showed an approximately threefold increase in efficiency under standard solar conditions and maintained superior performance in LED lighting, demonstrating enhanced adaptability and applicability in various lighting environments. These findings suggest that RGO acts as a conductive network that not only optimizes energy alignment at the interface but also minimizes recombination losses and improves overall carrier dynamics. The incorporation of RGO into ZnO offers a promising and scalable strategy to enhance the performance of perovskite solar cells. The RGO@ZnO-based device demonstrates a convincing balance between structural stability, high efficiency, and low-light operability, positioning it as a strong candidate for next-

generation photovoltaic applications, especially in environments requiring both outdoor and indoor energy harvesting. This work provides valuable insights into the material-level changes required to achieve high-performance, reliable, and application-flexible perovskite solar technologies.

Acknowledgments:

This work was supported by a grant from the Scientific Research Projects Unit at Kahramanmaras Sutcu Imam University, project number "2021/3-27 M." Research Projects Unit (Project Number: 2021/3-27M).

The author acknowledges Kahramanmaraş Sütçü İmam University, University-Industry-Public Collaboration Development Application and Research Center (ÜSKİM) for their valuable support during the experimental work and analyses. The author is also grateful to Saniye Tekerek for her invaluable assistance in the experimental procedures.

Author Contributions:

A. TANRIVERDİ: Conceptualization, Methodology, Investigation, Writing - Original Draft, Writing - Review & Editing, Supervision.

Funding:

Kahramanmaras Sutcu Imam University, Scientific Research Projects Unit, Project Number: "2021/3-27M"

Declarations:

Conflicts of Interest: The author declares that they have no competing financial interests or personal relationships that could have influenced the work reported in this article.

1. Chavan R.D., Wolska-Pietkiewicz M., Prochowicz D., et al. "Organic Ligand-Free ZnO Quantum Dots for Efficient and Stable Perovskite Solar Cells", *Adv. Funct. Mater.*, **32**(49), 2205909 (2022). DOI: 10.1002/adfm.202205909

2. Shakoor A., Nowsherwan G.A., Alam W., et al. "Fabrication and characterization of TiO_2:ZnO thin films as electron transport material in perovskite solar cell (PSC)", *Physica B: Condens. Matter*, **654**, 414690 (2023). DOI: 10.1016/j.physb.2023.414690

3. Saliba M., Correa-Baena J.P. and Grätzel M., "Perovskite solar cells: from the atomic level to film quality and device performance", *Angew. Chem. Int. Ed.*, **57**(10), 2554–2569 (2018). DOI: 10.1002/anie.201703226

4. Brooks K., "Perovskite", *Geol. Today*, **36**(1), 33–38 (2020). DOI: 10.1111/gto.12299

5. Ahmed S.F., Islam N., Kumar P.S., et al. "Perovskite solar cells: Thermal and chemical stability improvement, and economic analysis", *Mater. Today Chem.*, **27**, 101284 (2023). DOI: 10.1016/j.mtchem.2022.101284

6. Wang D., Wright M. and Elumalai N.K., "Stability of perovskite solar cells", *Sol. Energy Mater. Sol. Cells*, **147**, 255–275 (2016). DOI: 10.1016/j.solmat.2015.12.025

7. Kone K.E., Bouich A. and Marí-Guaita J., "Insight into the effect of halogen X in methylammonium lead halide ($MAPbX_3$) spin-coated on zinc oxide film", *Opt. Mater.*, **135**, 113238 (2023). DOI: 10.1016/j.optmat.2022.113238

8. Khan Z., Noman M., Jan S.T., et al. "Systematic investigation of the impact of kesterite and zinc based charge transport layers on the device performance and optoelectronic properties of ecofriendly tin (Sn) based perovskite solar cells", *Sol. Energy*, **257**, 58–87 (2023). DOI: 10.1016/j.solener.2023.04.019

9. Taheri-Ledari R., Valadi K. and Maleki A., "High-performance HTL-free perovskite solar cell: An efficient composition of ZnO NRs, RGO, and $CuInS_2$ QDs, as electron-transporting layer matrix", *Prog. Photovolt: Res. Appl.*, **28**(9), 956–970 (2020). DOI: 10.1002/pip.3306

10. Roose B., Tennyson E.M., Meheretu G., et al. "Local manufacturing of perovskite solar cells, a game-changer for low- and lower-middle income countries?", *Energy Environ. Sci.*, **15**(9), 3571–3582 (2022). DOI: 10.1039/D2EE01343F

11. Madurani K.A., Suprapto S. and Machrita N.I., et al. "Progress in graphene synthesis and its application: history, challenge and the future outlook for research and industry", *ECS J. Solid State Sci. Technol.*, **9**(9), 093013 (2020). DOI: 10.1149/2162-8777/abbb6f

12. Fatma I., Assad H. and Kumar A., "Introduction to Two-Dimensional Nanomaterials: Discovery, Types and Classifications, Structure, Unique Properties, and Applications", *Two-Dimensional Nanomaterials-Based Polymer Nanocomposites: Processing, Properties and Applications*, pp. 1–45 (2024). DOI: 10.1002/9781119905110.ch1

13. Choi J.H., Lee C. and Cho S., et al. "High capacitance and energy density supercapacitor based on biomass-derived activated carbons with reduced graphene oxide binder", *Carbon*, **132**, 16–24 (2018). DOI: 10.1016/j.carbon.2018.01.105

14. Saeed M.H., Alduwaib S.M. and Al-den D.J., "Investigation of structural, photo-luminescence and self-cleaning properties of thin layers of GO-ZnO and GO, GO-Ag and composite bilayer of GO-ZnO/GO-Ag prepared by spray pyrolysis method", *Scientia Iranica*, **31**(12), 958–966 (2024). DOI: 10.24200/sci.2023.61099.7140

15. Quevedo Robles R.V., Santana Camacho D. and Vilchis Nestor A.R., et al. "Role of natural extracts on the synthesis and properties of semiconductor nanoparticles of ZnO applied in water treatment by photocatalytic processes", *J. Mater. Sci.: Mater. Electron.*, **35**(11), 757 (2024). DOI: 10.1007/s10854-024-12505-8

16. Khan M.T. and Khan F., "Enhancement in photovoltaic performance of perovskites solar cells through modifying the electron transport layer with reduced graphene oxide", *Mater. Lett.*, **323**, 132578 (2022).DOI: 10.1016/j.matlet.2022.132578

17. Eswaramoorthy N. and Rajaram K., "1D graphitic carbon nitride additive modified ZnO electron transport layer for planar perovskite solar cells: 12.22% power conversion efficiency over 1 cm^2 active area", *Diamond Relat. Mater.*, **136**, 109917 (2023). DOI: 10.1016/j.diamond.2023.109917

18. Chaudhary A.K., Verma S. and Chauhan R.K., "Thermal and power performance optimization of cost-effective solar cells using eco-friendly perovskite materials", *Phys. Scr.*, **99**(2), 025512 (2024).. DOI: 10.1088/1402-4896/ad196e

19. Chauhan A., Kumar A. and Deolia V.K., "Zinc oxide doped with graphene quantum dots as improved electron transport layers for planner perovskite solar cells", *Int. J. Mod. Phys. B*, **39**(08), 2550058 (2025). DOI: 10.1142/S0217979225500584

20. Biswal H.J., Vundavilli P.R., Mondal K., et al. "ZnO/CuO nanostructures anchored over Ni/Cu tubular films via pulse electrodeposition for photocatalytic and antibacterial applications", *Mater. Sci. Energy Technol.*, **6**, 237–251 (2023). DOI: 10.1016/j.mset.2023.01.001

21. Ben Amor I., Hemmami H., Laouini S.E., et al. "Sol-gel synthesis of ZnO nanoparticles using different chitosan sources: effects on antibacterial activity and photocatalytic degradation of AZO Dye", *Catalysts*, **12**(12), 1611 (2022). DOI: 10.3390/catal12121611

22. MuthuKathija M., Badhusha M.S.M., and Rama V. "Green synthesis of zinc oxide nanoparticles using Pisonia Alba leaf extract and its antibacterial activity", *Applied Surface Science Advances*, **15**, 100400 (2023). DOI: 10.1016/j.apsadv.2023.100400

23. Ejsmont A. and Goscianska J. "Hydrothermal synthesis of ZnO superstructures with controlled morphology via temperature and pH optimization", *Materials*, **16**(4), 1641 (2023). DOI: 10.3390/ma16041641

24. Arun M., Rajendran I., and Senthil Kumar A.P. "Biosynthesis of silver nanoparticles using Histiopteris incisa leaf extract and their characterization and thermophysical study", *Scientia Iranica*, **32**(3) (2025). DOI: 10.24200/sci.2024.61386.7280

25. Alver Ü. and Tanrıverdi A. "Boron doped ZnO embedded into reduced graphene oxide for electrochemical supercapacitors", *Applied Surface Science*, **378**, 368–374 (2016). DOI: 10.1016/j.apsusc.2016.04.015

26. Rajguru G.M., Mishra R.K., Kharat P.B., and Khirade P.P. "Structural, microstructural and optical characteristics of rGO-ZnO nanocomposites via hydrothermal approach", *Optical Materials*, **154**, 115720 (2024). DOI: 10.1016/j.optmat.2024.115720

27. Tekerek S., Tanrıverdi A., Kiray E., et al. "Biological activities of boron and reduced graphene oxide-based zinc oxide nanocomposites (ZnO:B and RGO/ZnO:B) synthesized by an environmentally friendly method", *Brazilian Journal of Physics*, **54**(2), 35 (2024). DOI: 10.1007/s13538-023-01415-5

28. Bolaghi Z.K., Masoudpanah S.M., and Hasheminiasari M.J. "Photocatalytic activity of ZnO/RGO composite synthesized by one-pot solution combustion method", *Materials Research Bulletin*, **115**, 191–195 (2019). DOI: 10.1016/j.materresbull.2019.03.024

29. Boukhoubza I., Khenfouch M., Leontie L., et al. "Enhancement of the structural and morphological properties of ZnO/rGO nanocomposites synthesized by hydrothermal method", *Materials Today: Proceedings*, **53**, 324–331 (2022). DOI: 10.1016/j.matpr.2021.04.634

30. Padchasri J. and Yimnirun R. "Effects of annealing temperature on stability of methylammonium lead iodide perovskite powders", *Journal of Alloys and Compounds*, **720**, 63–69 (2017). DOI: 10.1016/j.jallcom.2017.05.170

31. Tsai Y.S., Chen J.R. and Lee C.H., "Morphologies and material properties of ZnO nanotubes, ZnO/ZnS core-shell nanorods, and ZnO/ZnS core-shell nanotubes", *Ceram. Int.* **48**[5] (2022) 7232–7239. DOI: 10.1016/j.ceramint.2021.11.283

32. Athar N., Naz G. and Ramzan M. et al., "Enhanced sunlight-driven photocatalysis owing to synergetic effect of gold nanoparticles-incorporated ZnO/rGO ternary heterostructures", *J. King Saud Univ. Sci.* **36**[3] (2024). DOI: 10.1016/j.jksus.2024.103104

33. Narzary R., Chetia R. and Sahu P.P., "A low-temperature efficient approach for the fabrication of ZnO-rGO heterostructures for applications in optoelectronic applications", *IEEE Access* **11** (2023) 80716–80725.DOI: 10.1109/ACCESS.2023.3300261

34. Narayanan G.N., Ananthasubramanian P. and Rajendran A.R. et al., "Hydrothermally synthesized ZnO and Z-rGO nanorods: Effect of post-annealing temperature and rGO incorporation on hydrogen sensing", *J. Mater. Sci. Mater. Electron.* **33**[12] (2022) DOI: 10.1007/s10854-021-07439-4

35. Tekerek S., "$MAIPbI_2$ perovskite solar cells fabricated based on the TiO_2, RGO@TiO_2, and SnO_2:F electron transport layers", *J. Nanopart. Res.* **26**[9] (2024) 216. DOI: 10.1007/s11051-024-06120-1

36. Manukyan K.V., Yeghishyan A.V. and Moskovskikh D.O. et al., "Mechanochemical synthesis of methylammonium lead iodide perovskite", *J. Mater. Sci.* **51**[19] (2016) 9123–9130. DOI: 10.1007/s10853-016-0165-4

37. Wang H., Zhang X. and Huang T. et al., "Enhance the performance of ZnO-based perovskite solar cells under ambient conditions", *Opt. Mater.* **89** (2019) 375–381. DOI: 10.1016/j.optmat.2019.01.059

38. Qasim I., Ahmad O. and Rashid A. et al., "Numerical optimization of (FTO/ZnO/CdS/$CH_3NH_3SnI_3$/GaAs/Au) perovskite solar cell using solar capacitance simulator with efficiency above 23% predicted", *Opt. Quantum Electron.* **53**[12] (2021) 713. DOI: 10.1007/s11082-021-03361-5

39. Singh R., Parashar M. and Sandhu S. et al., "The effects of crystal structure on the photovoltaic performance of perovskite solar cells under ambient indoor illumination", *Sol. Energy* **220** (2021) 43–50. DOI: 10.1016/j.solener.2021.01.052

40. Rashed S., Kutwade V.V. and Gattu K.P. et al., "Growth and Exploration of Inorganic Semiconductor Electron and Hole Transport Layers for Low-Cost Perovskite Solar Cells", *Trends Sci.* **20**[10] (2023) 5839. DOI: 10.48048/tis.2023.5839

41. Singh R., Shukla V.K. and Parashar M. et al., "Highly efficient quasi-cubic structured perovskite for harvesting energy from artificial indoor LED light source", *Sol. Energy* **245** (2022) 332–339. DOI: 10.1016/j.solener.2022.09.015

42. Esen V., Sağlam Ş. and Oral B., "Light sources of solar simulators for photovoltaic devices: A review", *Renew. Sustain. Energy Rev.* **77** (2017) 1240–1250. DOI: 10.1016/j.rser.2017.03.062

43. Hao M.Y., Wang H.Y. and Wang Y. et al., "Effect of energetic distribution of trap states on fill factor in perovskite solar cells", *J. Power Sources* **479** (2020) 229077.DOI: 10.1016/j.jpowsour.2020.229077

44. Le T.N., Le V.C. and Nguyen T.T.M. et al., "Synthesis of zinc oxide/reduced graphene oxide composites for fabrication of anodes in dye-sensitized solar cells", *Chem. Eng.* **78** (2020). DOI: 10.3303/CET2078011

45. Tavakoli M.M., Tavakoli R. and Yadav P. et al., "A graphene/ZnO electron transfer layer together with perovskite passivation enables highly efficient and stable perovskite solar cells", *J. Mater. Chem. A* **7**[2] (2019) 679–686. DOI: 10.1039/C8TA10857A

Biography

Ayça Tanrıverdi is an Assistant Professor at Kahramanmaraş Sütçü İmam University, Turkey, working at the Vocational School of Health Services in the Department of Medical Services and Techniques, Opticianry Program. She is also affiliated with the Department of Materials Science and Engineering at the same university. She obtained her PhD in Physics from the Graduate School of Natural and Applied Sciences, Kahramanmaraş Sütçü İmam University. She also completed her MSc in Physics (Thesis-based) and holds a BSc in Physics from the Faculty of Science and Letters at Kahramanmaraş Sütçü İmam University. Her research interests include materials physics, semiconductors, nanotechnology, and solar cells.

Figure Captions

Figure 1. Diagram of ZnO particle production process and experimental mechanism.

Figure 2. Perovskite solar cell in ITO/ZnO/$MAPbI_3$/PCBM/Ag and ITO/RGO@ZnO/ $MAPbI_3$/PCBM/Ag device structures

Figure 3. XRD pattern of ZnO NP and RGO@ZnO NC

Figure 4. SEM images of (a) ZnO NP and (b) RGO@ZnO NC

Figure 5. UV spectrum of ZnO NP and RGO@ZnO NC

Figure 6. Tauc plots of ZnO NP and RGO@ZnO NC

Figure 7. (a) XRD, (b) SEM, (c) UV and (d) Tauc plots of MAI.

Figure 8. (a) Current-voltage (J–V) and (b) power-voltage (P–V) graphs of the ITO/ZnO/$MAPbI_3$/PCBM/Ag device

Figure 9. (a) Current-voltage (J–V) and (b) power-voltage (P–V) graphs of the ITO/RGO@ZnO/$MAPbI_3$/PCBM/Ag device

Table Caption

Table 1. Photovoltaic parameters of ZnO and RGO@ZnO ETLs of perovskite solar cells

Figure 1. Diagram of ZnO particle production process and experimental mechanism.

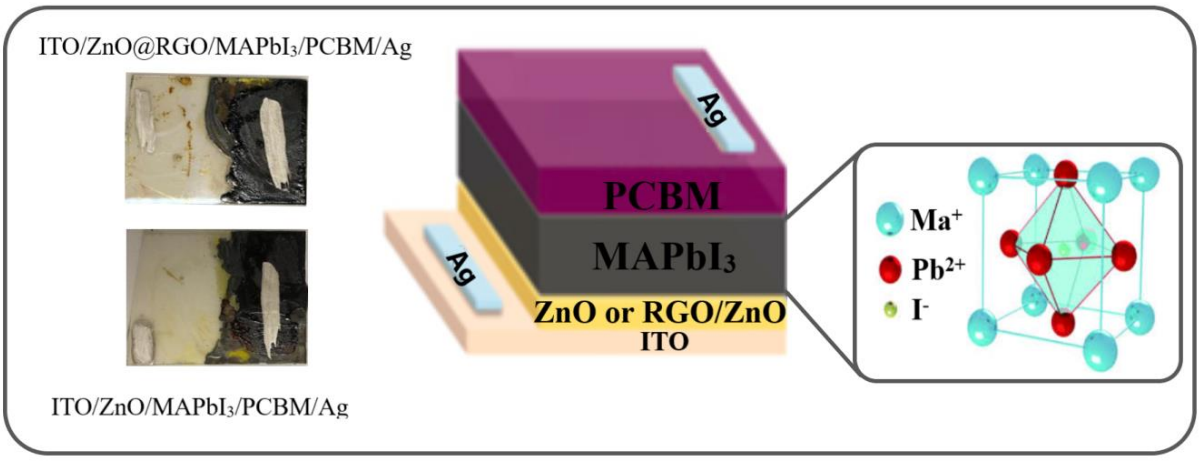

Figure 2. Perovskite solar cell in ITO/ZnO/$MAPbI_3$/PCBM/Ag and ITO/RGO@ZnO/ $MAPbI_3$/PCBM/Ag device structures

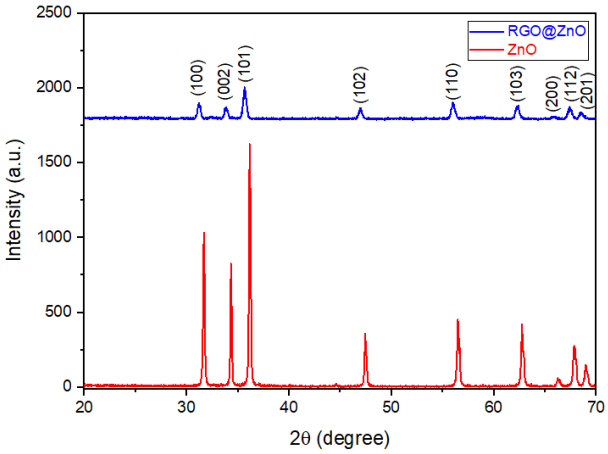

Figure 3. XRD pattern of ZnO NP and RGO@ZnO NC

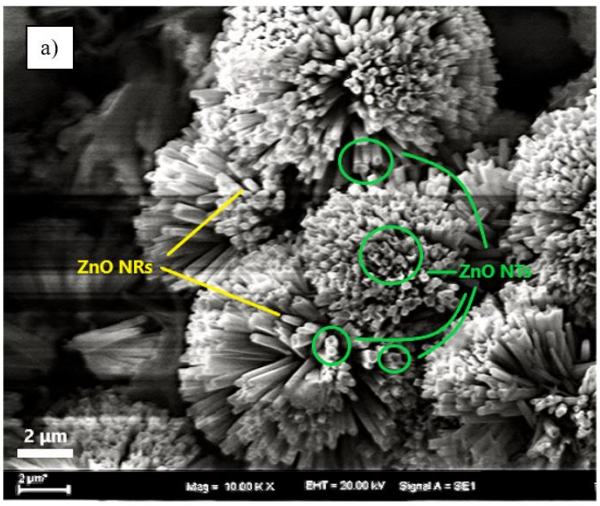

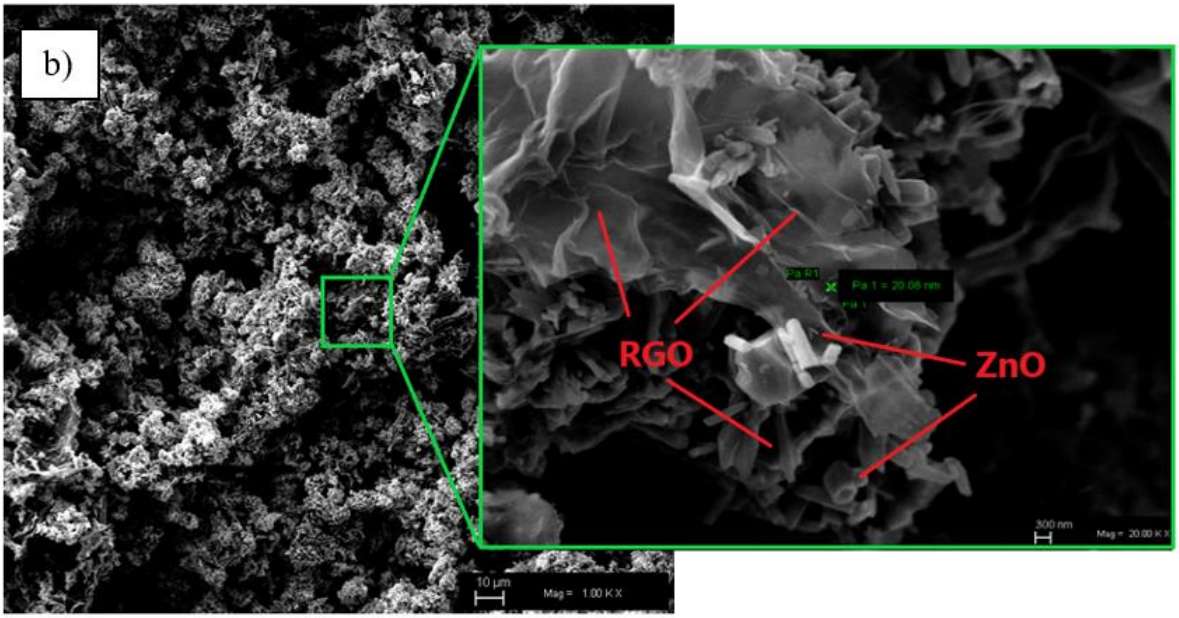

Figure 4. SEM images of (a) ZnO NP and (b) RGO@ZnO NC

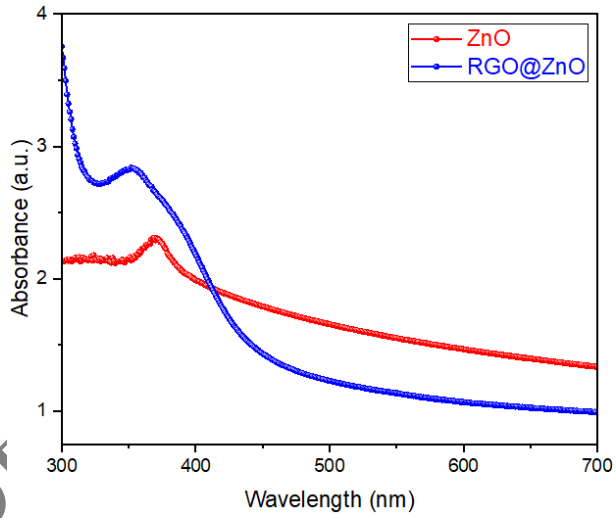

Figure 5. UV spectrum of ZnO NP and RGO@ZnO NC

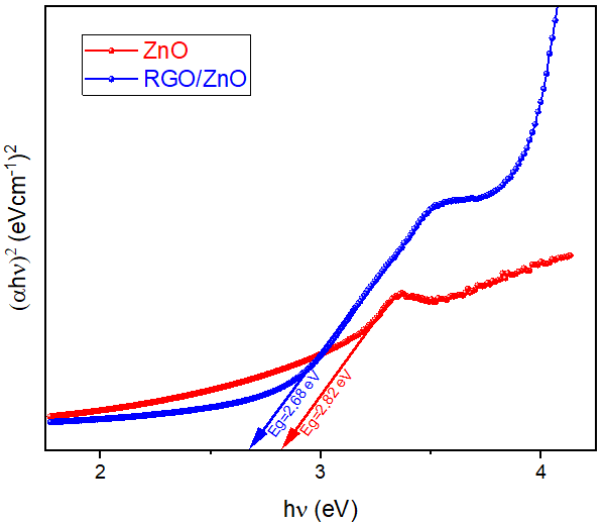

Figure 6. Tauc plots of ZnO NP and RGO@ZnO NC

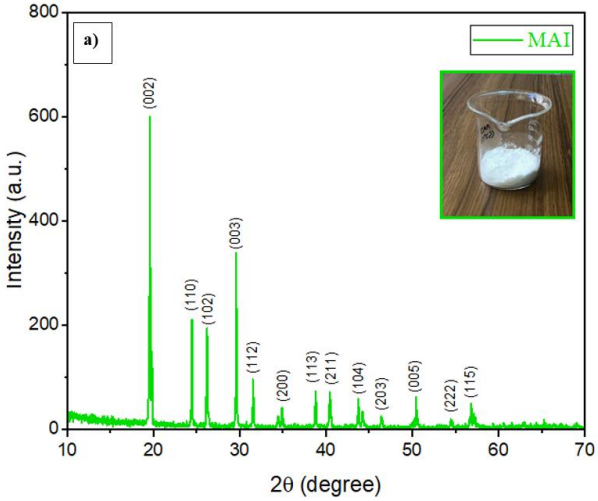

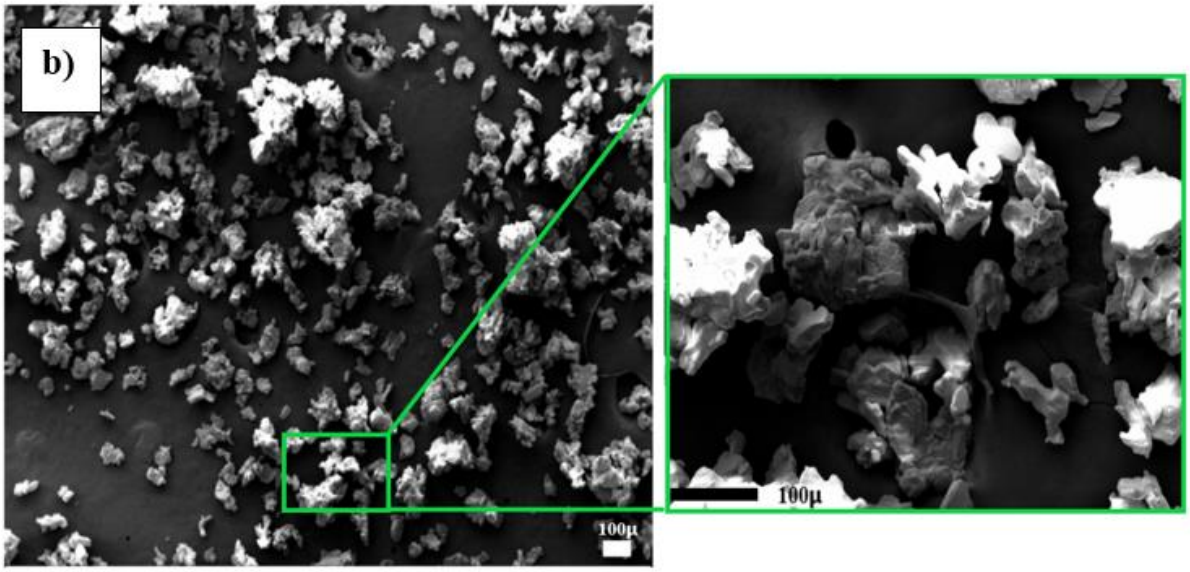

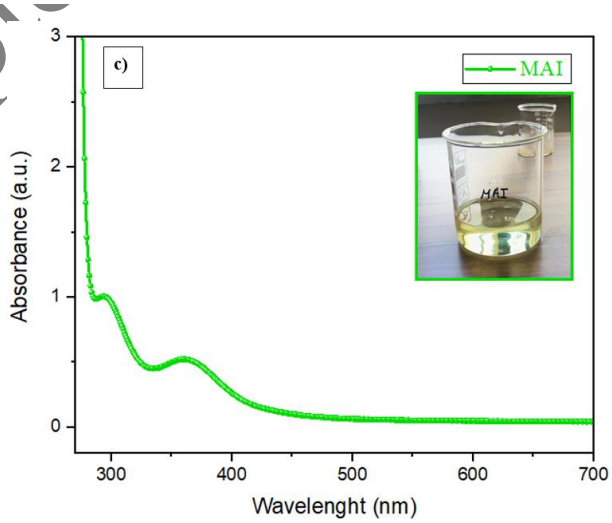

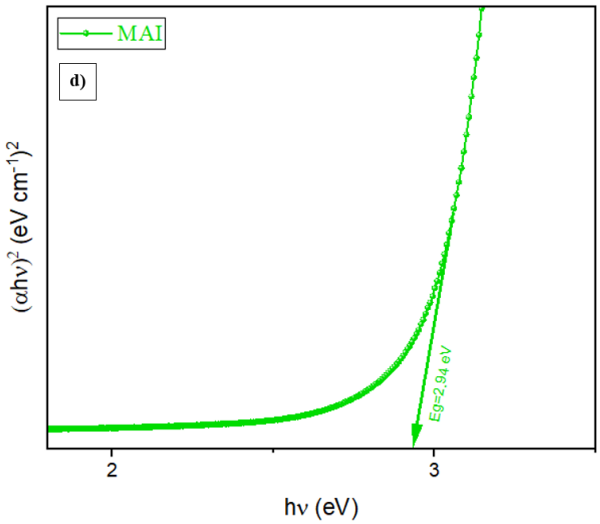

Figure 7. (a) XRD, (b) SEM, (c) UV and (d) Tauc plots of MAI.

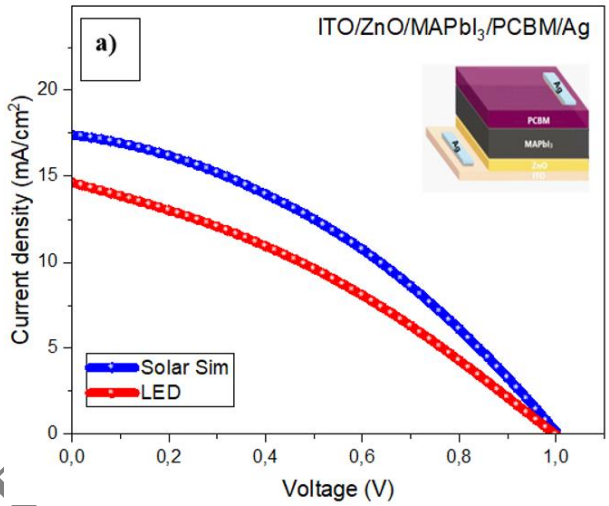

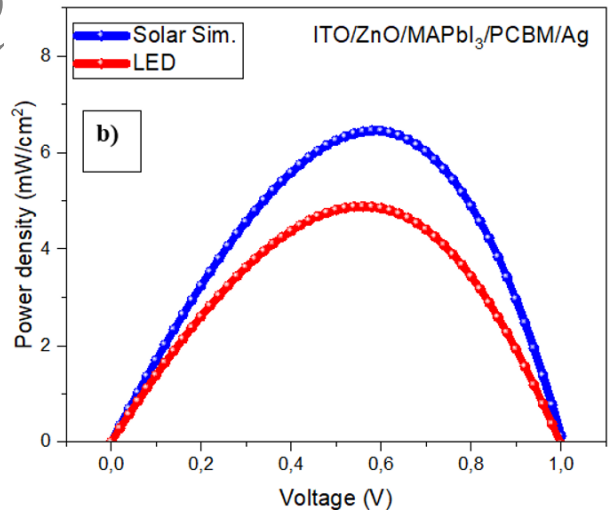

Figure 8. (a) Current-voltage (J–V) and (b) power-voltage (P–V) graphs of the ITO/ZnO/$MAPbI_3$/PCBM/Ag device

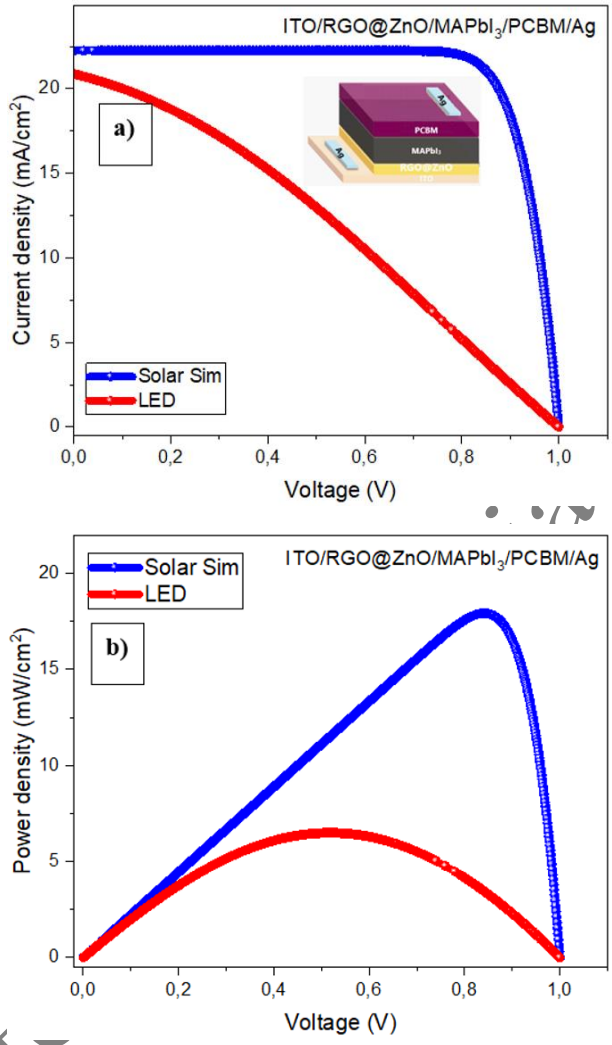

Figure 9. (a) Current-voltage (J–V) and (b) power-voltage (P–V) graphs of the ITO/RGO@ZnO/$MAPbI_3$/PCBM/Ag device

Table 1. Photovoltaic parameters of ZnO and RGO@ZnO ETLs of perovskite solar cells

Device Structure	Light Source	J_{SC} (mA/cm²)	V_{OC} (V)	*FF*	η (%)
ZnO	Solar Simulator	17.33	1.00	0.37	6.45
	LED	14.63	0.98	0.34	4.89
RGO@ZnO	Solar Simulator	22.24	1.00	0.80	17.93
	LED	20.87	0.99	0.31	6.50